nature photonics

LETTERS

PUBLISHED ONLINE: 20 JANUARY 2013 | DOI: 10.1038/NPHOTON.2012.329

Marker-free phase nanoscopy

Yann Cotte[1]*, Fatih Toy[1], Pascal Jourdain[2], Nicolas Pavillon[1], Daniel Boss[1,2], Pierre Magistretti[2,3], Pierre Marquet[2,3] and Christian Depeursinge[1]

We introduce a microscopic method that determines quantitative optical properties beyond the optical diffraction limit and allows direct imaging of unstained living biological specimens. In established holographic microscopy, complex fields are measured using interferometric detection, allowing diffraction-limited phase measurements. Here, we show that non-invasive optical nanoscopy can achieve a lateral resolution of 90 nm by using a quasi-2π-holographic detection scheme and complex deconvolution. We record holograms from different illumination directions on the sample plane and observe subwavelength tomographic variations of the specimen. Nanoscale apertures serve to calibrate the tomographic reconstruction and to characterize the imaging system by means of the coherent transfer function. This gives rise to realistic inverse filtering and guarantees true complex field reconstruction. The observations are shown for nanoscopic porous cell frustule (diatoms), for the direct study of bacteria (*Escherichia coli*), and for a time-lapse approach to explore the dynamics of living dendritic spines (neurones).

In the field of optical nanoscopy, image resolution at the subdiffraction scale has been obtained through saturation of fluorophore transitions[1] and has been demonstrated to work well with certain fluorescent proteins. Subdiffraction resolution has also been shown without using saturated fluorescence[2]. Although both techniques rely on phase structuring, it is used only in excitation. On its own, phase analysis provides a complementary means to fluorescence of measuring the morphology and composition of a specimen; additionally, quantitative phase analysis allows the study of the sample-induced optical path length (OPL) and the refractive index[3–5]. Recently, the determination of these parameters has become increasing important throughout the life sciences[6–9].

Here, we present marker-free and time-lapse phase nanoscopy, which allows lateral phase resolution below the 100 nm barrier. This can deal with the complex electromagnetic wave field scattered by a specimen, for example as obtained from the reconstruction of digitally recorded interferograms in digital holographic microscopy (DHM)[10] or, more generally, by various quantitative phase microscopy methods[11–13]. An appealing feature of reconstructed complex wave fields is the direct synthesis of the aperture of a virtual microscope[14–17]; that is, scattered light beyond the numerical aperture (NA) of the microscope objective (MO) can be detected, as described in Fig. 1a,b. Figure 1c shows a suitably engineered scanning concept for such a synthetic aperture. An inclined beam sequentially illuminates the specimen from various directions, thereby measuring the scattered field in the far-field regime for all possible directions of incidence. The goal is to match the 2π concept completely up to the free propagation limit (Fig. 1d–f) of the maximal wavenumber[18] $k_{max} = 2k = 4\pi n_i/\lambda$ for a given wavelength λ and immersion medium n_i. In the spatial frequency domain (SFD) of wave vector $\mathbf{k}$, each measurement of the scattered field represents a low-pass filtered (LPF) sub-aperture (S_i) as it suffers convolution with the system's three-dimensional coherent transfer function (CTF), depicted in Fig. 1g–i. Diffraction tomography[14] can be performed by synthesizing all three-dimensional SFD components S_i to obtain the LPF approximation (Fig. 1e) of the object's scattering potential[19], hereafter referred to as 'synthetic DHM'. In contrast to this LPF approach, the proposed method, termed 2π-DHM, uses complex deconvolved[20,21] sub-apertures O_i to effectively synthesize the scattering potential as far as k_{max} (Fig. 1f). In the 2π-DHM scanning concept, with two opposed high-NA MOs, complex deconvolution has the advantage of directly correcting (in the SFD) for any aberration[22,23] in phase (Fig. 1i) and apodization[24] in amplitude (Fig. 1h). Thanks to the combination of the physical detection of frequencies and the direct complex deconvolution model, 2π-DHM does not require any assumptions to be made concerning noise, iteration or sparsity[8].

If the synthetic bandpass is effectively enlarged up to the free propagation limit, then the resolution should improve significantly. The lateral resolution potential is determined by the total SFD content of the microscope ($2k_c$ in Fig. 1g), related to Abbe's formula $\eta_{min} = \alpha(\lambda/NA)$, where α yields 0.5 for the diffraction limit[24]. The effective resolution power between two scatterers at a distance η from one another is limited by the pointspread function (PSF), which implies a contrast of 27% (Rayleigh criterion[24] where α_{coh} yields 0.82 for coherent light) or 0% (Sparrow criterion[24]), as summarized in Supplementary Fig. S1 for different imaging modalities. With either criterion, the effective resolution of 2π-DHM is expected[18,25] to reach beyond the Abbe limit.

The setup for providing experimental proof for our method was based on a Mach–Zehnder interferometer[10], which provides quantitative phase images from a single-shot hologram for each illumination angle. A diode laser beam ($\lambda = 405$ nm) was divided into sample and reference arm paths by a beamsplitter. A wedge prism in imaging condition with an upright MO was used to rotationally scan the sample (positioned between the two matched oil-immersion MOs, NA = 1.4) at a steep angle of illumination (angle α in Fig. 1c). A second beamsplitter recombined the sample and reference laser beams, forming an off-axis interference pattern at the image plane. For each rotational angle of illumination (Euler angle φ in Fig. 1c, with angular sampling $\Delta\varphi \approx 1.5^\circ$), a charge-coupled device (CCD) camera (Basler 102f) recorded a hologram at 13.3 frames per second, providing a total of 240 holograms in 18 s for 360°. Phase images were then calculated by applying Fresnel reconstruction[10,26]. For complex deconvolution (see Methods), the CTF was derived experimentally by means of a complex point source (see Methods and Supplementary Figs S2,S3). All the deconvolved spectra were used consecutively for tomographic data processing (see Methods).

[1]Advanced Photonics Laboratory, Microvision and Microdiagnostic Group (SCI STI CHD), Ecole Polytechnique Fédérale de Lausanne (EPFL), 1015 Lausanne, Switzerland, [2]Brain and Mind Institute, Laboratory of Neuroenergetics and Cellular Dynamics (LNDC), Ecole Polytechnique Fédérale de Lausanne (EPFL), 1015 Lausanne, Switzerland, [3]Department of Psychiatry-University Hospital, Centre de Neurosciences Psychiatriques, 1008 Prilly-Lausanne, Switzerland.
*e-mail: yann.cotte@a3.epfl.ch

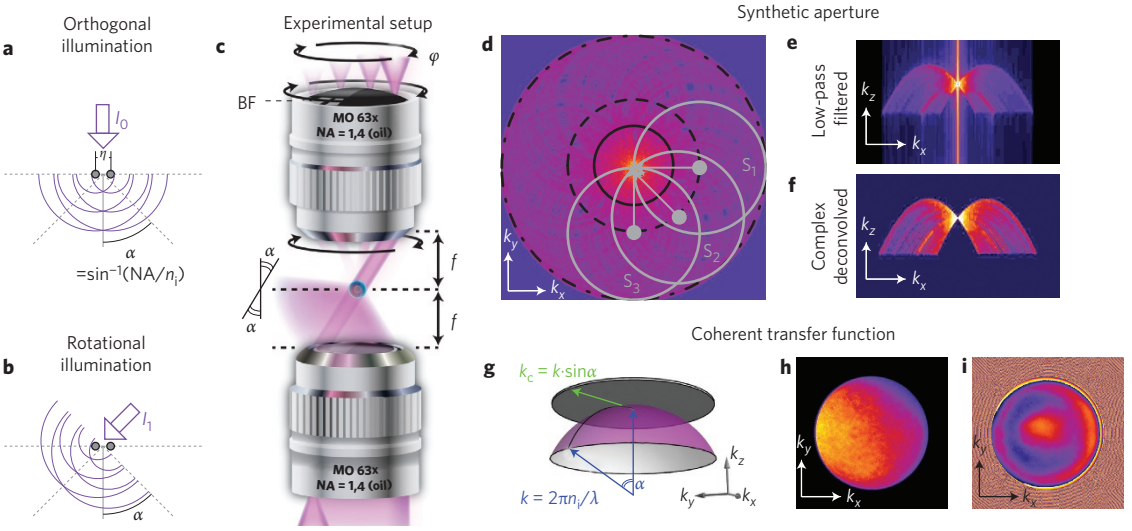

Figure 1 | Marker-free nanoscopy by 2π-DHM in real and spatial frequency domains. a, Two point scatterers are placed at a distance η from one another. The illumination light wave (I_0) produces a diffraction pattern, cut by the collection cone of the microscope objective (MO; NA, numerical aperture; n_i, immersion medium). **b**, Tilted illumination (I_1) shifts higher frequencies into the collection cone, thus providing the opportunity for improved resolution over regular DHM. **c**, Two opposed identical MOs can create steep illumination at an angle α from varying directions φ (f, working distance of MO; BF, back-focal plane). **d**, In SFD, each detected sub-aperture (S_i of an orientation φ) should sample a synthetic aperture beyond the diffraction limit in air (solid line) and in immersion (dashed line) up to the free propagation (2π) limit (dashed-dotted line). **e**, Without additional processing, the volume of the synthetic aperture remains low-pass filtered. **f**, In 2π-DHM, complex deconvolution by the CTF recovers the complete volume of the synthetic aperture up to the 2π limit. **g**, The three-dimensional CTF is given as the cap of a Ewald sphere, and its two-dimensional projection defines the cutoff frequency k_c of the bandwidth. **h**,**i**, Experimental measurement (by a complex point source as described in the Methods) of the two-dimensional projected CTF in amplitude (**h**) and phase (**i**) characterizes the imaging process.

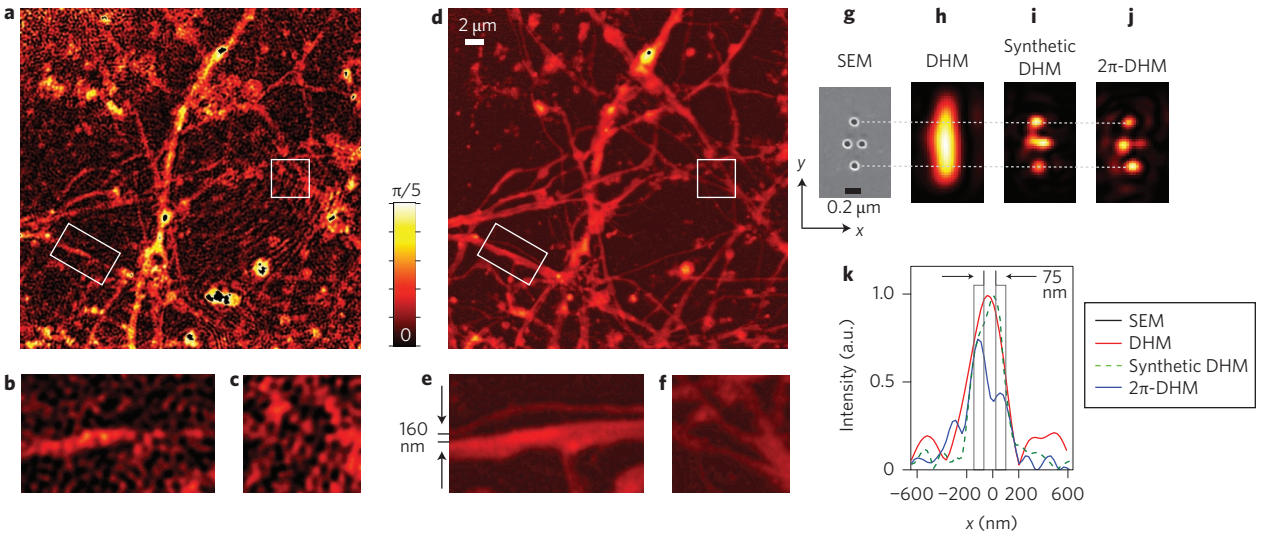

Figure 2 | Side-by-side comparisons of resolution in traditional DHM and 2π-DHM. a–**c**, The quantitative phase (full-field and magnifications of regions outlined by white squares) of a neuronal network is measured by traditional DHM in transmission configuration (NA = 1.4, λ = 405 nm). **d**–**f**, The super-resolved phase obtained by 2π-DHM reveals the spatial order of the self-assembled neural network. **g**, SEM image of the resolution target used for calibration, which consists of four nanometric holes (diameters, 75 nm). **h**–**j**, Their mutual distances are beneath the optical diffraction limit, as shown by the different imaging modalities. Only 2π-DHM resolves all the holes individually. **k**, Horizontal profile measurement, showing a 2π-DHM Sparrow resolution of 75 nm.

We first imaged unstained living mouse cortical neurons, and the 2π-DHM was found to produce a striking improvement in lateral resolution over conventional DHM (Fig. 2a–f). Single dendrites and interdendritic cavities have dimensions measuring less than 100 nm, indicating that the lateral phase resolution is at least of that order. The exact lateral resolution can be captured by a customized resolution test sample (for fabrication see Supplementary Fig. S3 and Supplementary Methods). The scanning electron microscopy (SEM) image in Fig. 2g confirms hole diameters of 75 nm and hole mutual rim-to-rim distances of $\eta_h = 75 \pm 5$ nm (horizontal) and $\eta_v = 425 \pm 5$ nm (vertical). Being limited to Rayleigh's limit of $\eta^{coh} \approx 240$ nm and a diffraction limit of $\eta^{Abbe} \approx 150$ nm, traditional DHM (Fig. 2h) fails to discern these structures. The LPF synthetic DHM (Fig. 2i) improves the resolution of vertical holes, but aberrations prevent the resolution of horizontal ones. In contrast, 2π-DHM (Fig. 2j–k) succeeds in separating individual holes and η_h indicates a lateral (Sparrow) resolution of 75 nm. Scanning of the specimen also suggests a spatial variation of noise[27], and reduces

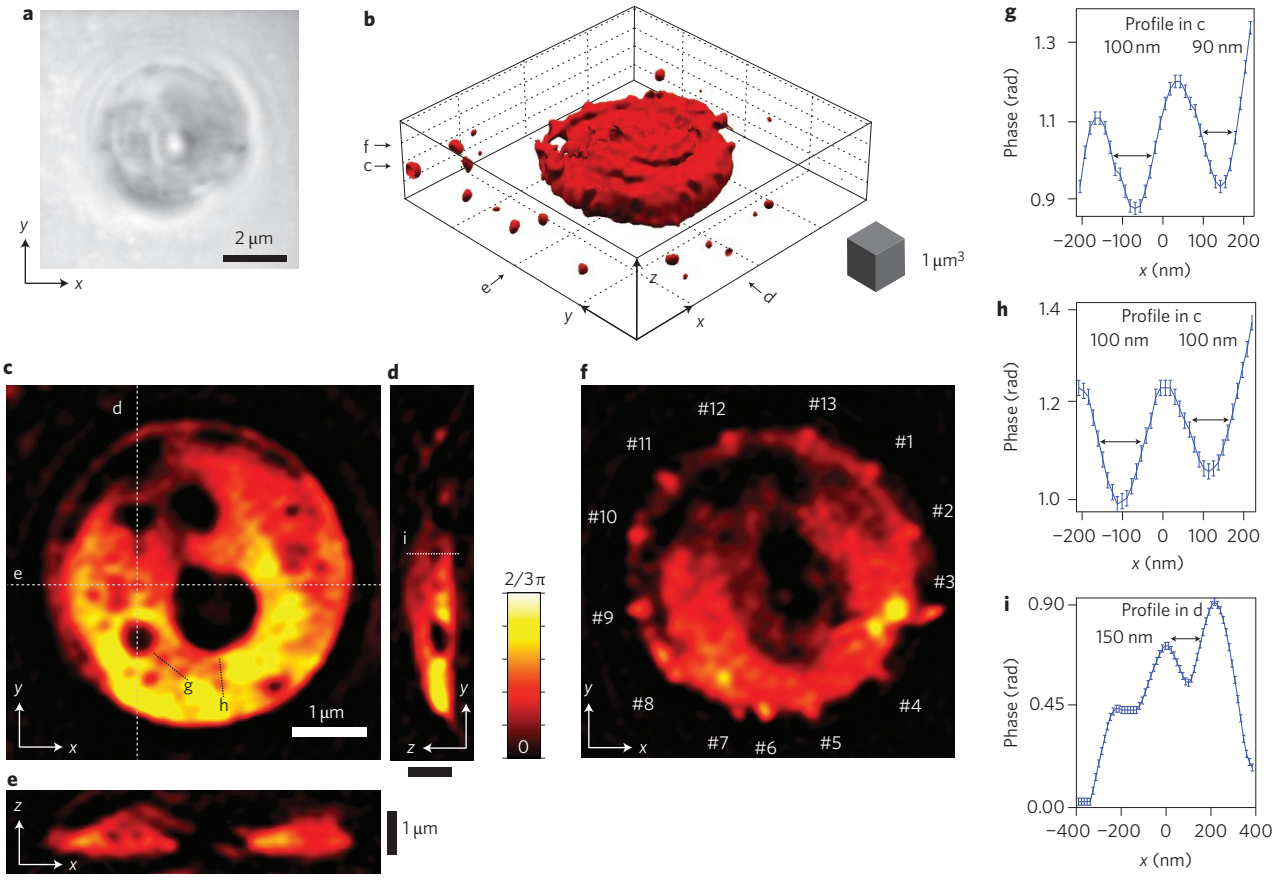

Figure 3 | Super-resolved phase images of nanoscopic porous cell frustule (diatoms). a, Amplitude image of a transparent diatom. **b**, Three-dimensional phase tomogram with arrows indicating sections. **c**, Central section, revealing inner porous structures measured by profiles and sections. **d**,**e**, Axial sections cut through the porous structures enclosed in the diatom. **f**, Planar section on the top of the diatom, featuring its annular crown structure with 13 portulae structures highlighted. **g**–**i**, Profile measurements of nanoscopic pores with sub-100 nm lateral resolution and an axial resolution of 150 nm with spatial noise error bars of $\sigma_\phi = \pm 0.9^\circ$.

phase noise σ_ϕ by one order of magnitude compared to traditional DHM. Thus, 2π-DHM features an axial phase precision of $\sigma_\phi = \pm 0.9^\circ$ or an OPL precision of 2 nm. Another difference between DHM and 2π-DHM concerns the phase, which in DHM derives from an integrated signal over the depth of field. The signal from 2π-DHM arises from diffraction tomography, and results therefore in optically sectioned phase images.

An excellent demonstration of diffractive tomographic phase comprises imaging of a three-dimensional specimen featuring sudden refractive index changes, such as nanoscopic porous *Thalassiosira pseudonana frustule* (the diatom cell in Fig. 3 and Supplementary Movie S1). Diatoms are one of the most common type of phytoplankton (Fig. 3a illustrates their transparent silica skeleton). The three-dimensional rendered tomogram of equiphase in Fig. 3b reveals its general shape and dimensions. The central section through the diatom shown in Fig. 3c demonstrates its inner architecture, which contains numerous inner portulae structures. The profile plots in Fig. 3g,h confirm a lateral resolution in the 100 nm range, in accordance with an earlier transmission electron microscopy (TEM) characterization[28] giving a diameter of 79 ± 14 nm. The section in Fig. 3f cuts through the top of the diatom, which features 13 typical rimoportulae of mean width 202 ± 26 nm, matching the TEM reference[28] of 176 ± 21 nm. Figure 3b reveals their three-dimensional positions, which are particularly prominent for rimoportulae nos 5–7. The axial sections through the diatom in Fig. 3d,e show variations in thickness, ranging from 0.5 µm to 1 µm, with enclosed circular vacancies.

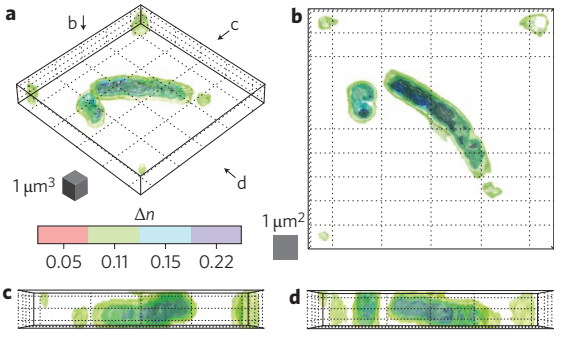

Figure 4 | Refraction tomogram of bacteria (*E. coli*). a–**d**, Perspective views along the directions indicated in **a** (arrows) with grouping in pseudo-colours of refractive index difference Δn.

The profile in Fig. 3i suggests the axial resolution to be on the order of $\eta^{\text{axial}} = 150$ nm.

Escherichia bacteria (*E. coli*) serve to demonstrate 2π-DHM as a tool for cell imaging. Figure 4 presents different three-dimensional perspective views of the tomographic variation in the refractive index in one such bacterium. Based on scattering potential theory[14,19], the quantitative tomographic phase is related to integration of the local refractive index[4,5]. As described earlier[21], we analysed the forward-scattered light in a direct model, that is, based on the first Born approximation[29]. The three-dimensional refractive

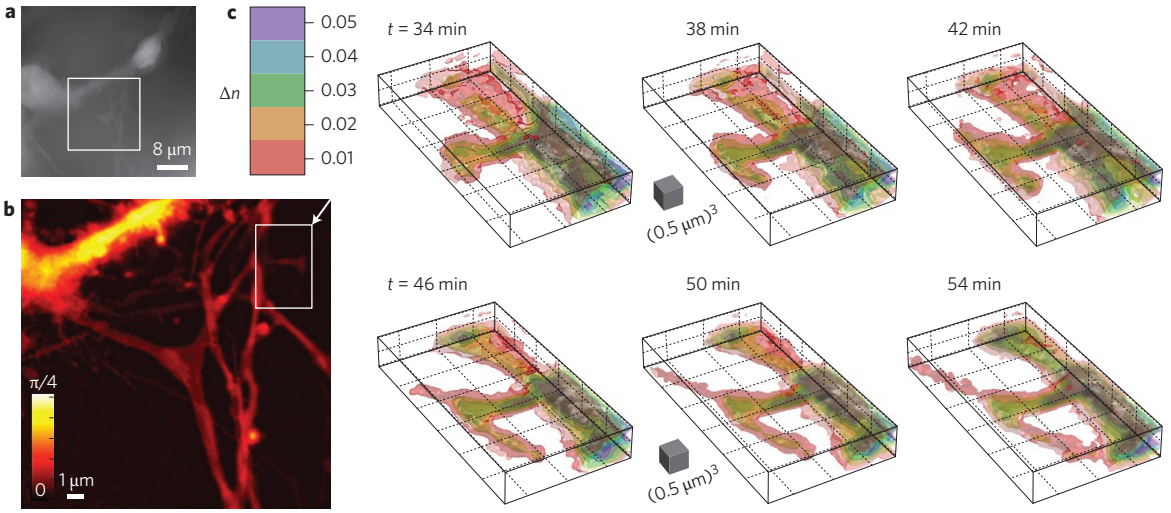

Figure 5 | Three-dimensional remodelling of a synaptic network from observations over a long time. a, Full field of view in phase, showing a pair of neurons. **b**, The magnified neural network in phase with the region of interest; arrow indicates the perspective for **c**. **c**, Time-lapsed refractive index change Δn during filopodia formation of a neuronal spine (perspective view).

index map illustrates well the general shape and intracellular content of the bacterium. The smallest detectable variation ($\delta_{\Delta n}$) of refractive index difference (Δn) for an optical section η^{axial} can be linearly estimated from the system's phase precision σ_ϕ to be sensitive down to $\delta_{\Delta n} = (\sigma_\phi/2\pi)(\lambda/\eta^{\text{axial}}) \approx \pm 0.007$.

With such high Δn sensitivity and spatial resolution, 2π-DHM is very well suited to visualizing nanometre-scale alterations in neural remodelling processes. We performed time-lapse imaging on five-day-old live mouse cortical neurons. Samples were observed directly (see Methods) without the need for preliminary preparation steps such as fixation, membrane permeabilization or fluorophore incubation. The absence of fluorophores removes any concerns regarding cytotoxicity, phototoxicity through bleaching and molecular oxidation, or phototoxicity from high-power laser intensities (the experimental power exposure has been estimated previously[7] not to exceed 0.1 W cm^{-2}). The full field of view of 50 × 50 µm^2 in Fig. 5a shows two neurons and their synaptic contact regions, which are magnified in Fig. 5b and Supplementary Movie S2. As described in the literature[30], during neuronal development, various synaptic network remodelling processes take place. In one-hour-long time-lapse imaging, we observed these processes every minute. As an example, Fig. 5c and Supplementary Movie S3 demonstrate the three-dimensional reconstruction of the filopodia of a spine dendrite. After initial refractive index augmentation (<42 min), a thin (~150 nm) dendrite grows on the upper side at a mean velocity of ~400 nm min^{-1} in a timescale of 8 min. On the lower side, it succeeds in establishing synaptic contact, accompanied by local refractive index (~100 nm away from the synapse) augmentation.

In summary, we have developed a technique for non-invasive marker-free quantitative nanoscopy of living cells and tissues. This method is based on super-resolved phase measurements, and has been shown to surpass the 100 nm lateral resolution barrier in wide field. Its quantitative nature allows the study of local refractive index variations related to the 2 nm precision of OPL, combined with high three-dimensional spatial resolution. Our measurements demonstrate the potential of 2π-DHM as a tool of great biological interest by showing its use in monitoring cell morphology and dynamics in non-invasive time-lapse measurements.

Methods

Complex point source(s). To create complex point sources, nanoscale apertures were illuminated coherently. Nanoscale apertures (hole diameter, 75 nm) were drilled into a thin opaque metal coating on a conventional microscopy coverslip (no. 1.5), resulting in a high signal-to-noise ratio (SNR). The apertures were fabricated by focused ion beam (FIB) milling through an evaporated aluminium film (thickness, 100 nm). The coherent imaging system can be experimentally characterized by a singular and isolated complex point source (Supplementary Fig. S2a), that is, using amplitude PSF (APSF) measurements. Using digital Fresnel reconstruction of the complex point source's hologram[10], a pseudo three-dimensional field was retrieved by varying the reconstruction distance d by $d' = d + M^2 z_1$ (M, lateral magnification of MO; z_1, in focus distance), as shown in Supplementary Fig. S2b. The DHM three-dimensional CTF was calculated by a three-dimensional fast Fourier transform (3D FFT), as depicted in Supplementary Fig. S2c. Groups of nanoscale apertures served as resolution (Fig. 2g) and tomographic calibration targets (Supplementary Fig. S5). For more details on fabrication see Supplementary Methods.

Tomographic data processing. The data processing comprised several iterative steps, as summarized in Supplementary Fig. S4. First, individual holograms were reconstructed based on Fresnel propagation[10], numerical lenses[26] and background subtraction. Second, a three-dimensional matrix was calculated by back-propagation, which means that the reconstruction distance d of the complex field was varied by $d' = d + M^2 z_1$. Third, a 3D FFT gave the three-dimensional LPF spectrum S_i. Fourth, the realistically inverse filtered spectra O_i were obtained by complex regularized three-dimensional complex deconvolution[21], as further outlined in Methods section 'Complex deconvolution'. Fifth, for synthesis of the object's scattering potential the individual spectra O_i were stitched; that is, caps of the deconvolved Ewald sphere (similar to Fig. 1g) were used to sample a volume in three-dimensional SFD (Fig. 1f). Considering that an orthogonal illumination (Fig. 1a) is presented by wave vector $\mathbf{k}_0'$ in the laboratory reference frame, rotational scanning (Fig. 1b–c) implies measurements in the direction of the inclined illumination wave vector $\mathbf{k}_0'$. Hence, the object's spectrum $O_i(\mathbf{K})$ was measured in the SFD of $\mathbf{K} = \mathbf{k} - \mathbf{k}_0$. For synthesis, each reconstruction $O_i(\mathbf{K})$ needs to be repositioned to $O_i'(\mathbf{K})$ relative to the laboratory reference frame (Fig. 1d). A direct and automated way of determining displacement matrix $\mathbf{f}(\mathbf{k}_0)$ for each component $O_i(\mathbf{K})$ consists in the detection of k_0 (given as the carrier frequency of O_i), as proposed earlier[14]. To guarantee effective super-resolution, it is crucial to validate the correctness of $\mathbf{f}(\mathbf{k}_0)$ for given illumination conditions by a novel experimental calibration technique (Supplementary Methods). These steps were iteratively and automatically repeated for N holograms of 360° illumination rotation. In this manner, the object's scattering potential O was sampled in three-dimensional SFD by means of inversely repositioned (calibrated) spectra O_i':

$$O(\mathbf{K}) = \sum_N O_i'(\mathbf{K}) = \sum_N \mathbf{f}^{-1}(\mathbf{k}_0) O_i(\mathbf{k} - \mathbf{k}_0) \quad (1)$$

In the final step, the reconstructed scattering potential in equation (1) was recast to real space by using equation (2),

$$o(\mathbf{r}_1) = \frac{1}{(2\pi)^3} \iiint_{K \le 2k} O(\mathbf{K}) \exp[\mathbf{K}\mathbf{r}_1] \mathrm{d}K_x \mathrm{d}K_y \mathrm{d}K_z \quad (2)$$

to reconstitute the tomographic object o in amplitude and phase.

Complex deconvolution. Deconvolution is the mathematical inversion of image formation. Based on coherent image formation and 3D FFT, the deconvolution can be expressed for coherent imaging as the division in SFD of complex spectrum $S_i(k)$ by the CTF $c(k)$:

$$o_i(\mathbf{r_1}) = \frac{1}{(2\pi)^3}\iiint O_i(\mathbf{K})\exp[i\mathbf{kr_1}]\mathrm{d}k_x\mathrm{d}k_y\mathrm{d}k_z = \frac{1}{(2\pi)^3}\iiint \frac{S_i(k)}{c(k)}\exp[i\mathbf{kr_1}]\mathrm{d}k_x\mathrm{d}k_y\mathrm{d}k_z \quad (3)$$

Equation (3) results in the object's spectrum $O_i(k)$ or, in real space, in the scattered object field $o_i(r_1)$. For realistic complex deconvolution, the three-dimensional CTF is experimentally acquired by a complex point source (it could alternatively be modelled as described elsewhere[20,21]). Phase deconvolution plays a key role in the treatment of complex fields. To avoid phase signal degradation by (amplitude) noise amplification, a bandpass filter[20] is applied to spectrum S_i. Axial noise degradation is effectively reduced by complex regularization[21] of the three-dimensional CTF in equation (3):

$$\tilde{c}(\mathbf{k}) = \begin{cases} c & \text{if } |c| > \tau \\ 1\cdot\exp\left[\mathrm{i}\cdot\arg[c]\right] & \text{if } |c| \le \tau \end{cases} \quad (4)$$

For a modulus of c smaller than the complex threshold τ, the CTF amplitude is set to unity, so that its noise amplification is eliminated while its phase value still acts for the deconvolution. The assessment of τ in equation (4) is automated by a histogram-based method—Otsu's rule.

Sample preparation. Diatom cells (*T. pseudonana frustule*) and thawed *Escherichia* bacteria (*E. coli*) were suspended in water. Five-day-old mouse cortical neurons were used; these were bathed in a HEPES-buffered standard physiological medium containing NaCl (140 mM), KCl (3 mM), $CaCl_2$ (3 mM), $MgCl_2$ (2 mM), glucose (5 mM) and HEPES (10 mM), adjusted to a pH of 7.3 with NaOH[31]. All samples were mounted between a pair of conventional microscopy coverslips (no. 1.5) separated by an adhesive imaging spacer (Grace Bio-Labs SS1X9-SecureSeal Imaging Spacer: inner diameter, 9 mm; thickness, 0.12 mm; 18 mm × 18 mm).

Received 30 July 2012; accepted 20 November 2012; published online 20 January 2013; corrected online 16 April 2013

References

1. Hell, S. W. Far-field optical nanoscopy. *Science* **316,** 1153–1158 (2007).
2. Gustafsson, M. G. L. Surpassing the lateral resolution limit by a factor of two using structured illumination microscopy. *J. Microsc.* **198,** 82–87 (2000).
3. Rappaz, B. *et al.* Measurement of the integral refractive index and dynamic cell morphometry of living cells with digital holographic microscopy. *Opt. Express* **13,** 9361–9373 (2005).
4. Charrière, F. *et al.* Living specimen tomography by digital holographic microscopy: morphometry of testate amoeba. *Opt. Express* **14,** 7005–7013 (2006).
5. Choi, W. *et al.* Tomographic phase microscopy. *Nature Methods* **4,** 717–719 (2007).
6. Kemper, B. *et al.* Investigation of living pancreas tumor cells by digital holographic microscopy. *J. Biomed. Opt.* **11,** 034005 (2006).
7. Pavillon, N. *et al.* Early cell death detection with digital holographic microscopy. *PLoS ONE* **7,** e30912 (2012).
8. Mir, M. *et al.* Visualizing *Escherichia coli* sub-cellular structure using sparse deconvolution spatial light interference tomography. *PLoS ONE* **7,** e39816 (2012).
9. Rappaz, B., Depeursinge, C. & Marquet, P. in *Biomedical Optical Phase Microscopy and Nanoscopy* (eds Shaked, N. T., Zalevskey, Z. & Satterwhite, L.) Ch. 5.1, 71–95 (Elsevier, 2012).
10. Cuche, E., Marquet, P. & Depeursinge, C. Simultaneous amplitude-contrast and quantitative phase-contrast microscopy by numerical reconstruction of Fresnel off-axis holograms. *Appl. Opt.* **38,** 6994–7001 (1999).
11. Gureyev, T. E., Roberts, A. & Nugent, K. A. Phase retrieval with the transport-of-intensity equation: matrix solution with use of Zernike polynomials. *J. Opt. Soc. Am. A* **12,** 1932–1941 (1995).
12. Popescu, G. in *Methods in Nano Cell Biology* vol. 90 (eds Jena, B. P.) 87–115 (Academic, 2008).
13. Bon, P., Maucort, G., Wattellier, B. & Monneret, S. Quadriwave lateral shearing interferometry for quantitative phase microscopy of living cells. *Opt. Express* **17,** 13080–13094 (2009).
14. Lauer, V. New approach to optical diffraction tomography yielding a vector equation of diffraction tomography and a novel tomographic microscope. *J. Microsc.* **205,** 165–176 (2002).
15. Paturzo, M. *et al.* Super-resolution in digital holography by a two-dimensional dynamic phase grating. *Opt. Express* **16,** 17107–17118 (2008).
16. Mico, V., Zalevsky, Z., Ferreira, C. & García, J. Superresolution digital holographic microscopy for three-dimensional samples. *Opt. Express* **16,** 19260–19270 (2008).
17. Debailleul, M., Georges, V., Simon, B., Morin, R. & Haeberle, O. High-resolution three-dimensional tomographic diffractive microscopy of transparent inorganic and biological samples. *Opt. Lett.* **34,** 79–81 (2009).
18. Kuznetsova, Y., Neumann, A. & Brueck, S. R. J. Solid-immersion imaging interferometric nanoscopy to the limits of available frequency space. *J. Opt. Soc. Am. A* **29,** 772–781 (2012).
19. Devaney, A. A filtered backpropagation algorithm for diffraction tomography. *Ultrason. Imaging* **4,** 336–350 (1982).
20. Cotte, Y., Toy, M. F., Pavillon, N. & Depeursinge, C. Microscopy image resolution improvement by deconvolution of complex fields. *Opt. Express* **18,** 19462–19478 (2010).
21. Cotte, Y. *et al.* Realistic 3D coherent transfer function inverse filtering of complex fields. *Biomed. Opt. Express* **2,** 2216–2230 (2011).
22. Sheppard, C. J. R. & Gu, M. Imaging by a high aperture optical-system. *J. Mod. Opt.* **40,** 1631–1651 (1993).
23. Vertu, S., Flagge, J., Delaunay, J.-J. & Haeberle, O. Improved and isotropic resolution in tomographic diffractive microscopy combining sample and illumination rotation. *Cent. Eur. J. Phys.* **9,** 969–974 (2011).
24. den Dekker, A. J. & van den Bos, A. Resolution: a survey. *J. Opt. Soc. Am. A* **14,** 547–557 (1997).
25. Cotte, Y., Toy, M. F. & Depeursinge, C. Beyond the lateral resolution limit by phase imaging. *J. Biomed. Opt.* **16,** 106007 (2011).
26. Montfort, F. *et al.* Purely numerical compensation for microscope objective phase curvature in digital holographic microscopy: influence of digital phase mask position. *J. Opt. Soc. Am. A* **23,** 2944–2953 (2006).
27. Choi, Y., Yang, T. D., Lee, K. J. & Choi, W. Full-field and single-shot quantitative phase microscopy using dynamic speckle illumination. *Opt. Lett.* **36,** 2465–2467 (2011).
28. Hildebrand, M. *et al.* Nanoscale control of silica morphology and three-dimensional structure during diatom cell wall formation. *J. Mater. Res.* **21,** 2689–2698 (2006).
29. Sheppard, C. J. R., Kou, S. S. & Depeursinge, C. Reconstruction in interferometric synthetic aperture microscopy: comparison with optical coherence tomography and digital holographic microscopy. *J. Opt. Soc. Am. A* **29,** 244–250 (2012).
30. Portera-Cailliau, C., Pan, D. T. & Yuste, R. Activity-regulated dynamic behavior of early dendritic protrusions: evidence for different types of dendritic filopodia. *J. Neurosci.* **23,** 7129–7142 (2003).
31. Tao, H.-z. *et al.* Selective presynaptic propagation of long-term potentiation in defined neural networks. *J. Neurosci.* **20,** 3233–3243 (2000).

Acknowledgements

This work was funded by the Swiss National Science Foundation (SNSF, grant no. 205 320–130 543) and EPFL (innovation grant INNO 12-14). The authors acknowledge the Center of MicroNano-Technology (CMI) for cooperation regarding its research facilities. The authors give special thanks to M. Hildebrand for providing diatom samples, and to L. Pollaro for preparing the *E. coli* samples. The authors also thank P. Lara Rodrigo, C-M. Cotte and Cemico GmbH for assistance with graphics. Finally, the authors thank E. Cuche, CTO of Lyncée Tec, for helpful discussions and suggestions.

Author contributions

Y.C., F.T., N.P. and C.D. designed the experiments. Y.C. and F.T. performed the experiments and carried out the main data analysis. P.J. and D.B. prepared the biological samples. C.D. and P.Mar. provided overall guidance to the project. All authors discussed the results and contributed to the manuscript.

Additional information

Supplementary information is available in the online version of the paper. Reprints and permission information is available online at http://www.nature.com/reprints. Correspondence and requests for materials should be addressed to Y.C.

Competing financial interests

Yann Cotte, Nicolas Pavillon and Christian Depeursinge are named inventors on international patent WO/2011/121523 (publication date 06.10.2011, international filing date 28.03.2011), which is related to the techniques described in this Letter.

CORRIGENDUM

Marker-free phase nanoscopy

Yann Cotte, Fatih Toy, Pascal Jourdain, Nicolas Pavillon, Daniel Boss, Pierre Magistretti, Pierre Marquet & Christian Depeursinge

Nature Photon. **7,** 113–117 (2013); published online 20 January 2013; corrected online 16 April 2013.

In the version of this Letter originally published online, no competing financial interests were declared. However, the authors wish to acknowledge a relevant patent. The competing financial interests statement has been modified as shown below in the HTML and PDF versions of the Letter:

Yann Cotte, Nicolas Pavillon and Christian Depeursinge are named inventors on international patent WO/2011/121523 (publication date 06.10.2011, international filing date 28.03.2011), which is related to the techniques described in this Letter.